

*Proceedings of the Twenty-fifth (2015) International Ocean and Polar Engineering Conference
Kona, Big Island, Hawaii, USA, June 21-26, 2015
Copyright © 2015 by the International Society of Offshore and Polar Engineers (ISOPE)
ISBN 978-1-880653-89-0; ISSN 1098-6189*

www.isopec.org

Coordinated Motion Control of a 3-Link Dual-Arm Underwater Vehicle-Manipulator System Using Resolved Acceleration Control Method

Radzi Bin Ambar Shinichi Sagara
Department of Mechanical and Control Engineering
Kyushu Institute of Technology
Kitakyushu, Fukuoka, Japan

Fumiaki Takemura
Department of Mechanical System Engineering
Okinawa National College of Technology
Nago, Okinawa, Japan

ABSTRACT

This paper presents a digital resolved acceleration control method for coordinated motion control of an underwater vehicle equipped with manipulators. Using this method, in spite of large position and attitude errors of the underwater vehicle, good control performances of the end-tips of the manipulators to follow a pre-planned trajectory can be achieved. In this work, theoretical work of the proposed method is described. Then, the effectiveness of the proposed method is demonstrated through experimental work using a 3-link dual-arm underwater robot in actual underwater environment.

KEY WORDS: Underwater vehicle; manipulator; UVMS; resolved acceleration; control.

INTRODUCTION

The current research in the field of robotics has expanded significantly from industry related robots, to robots that can operate in extreme environments such as deep underwater environment. Nowadays, unmanned underwater vehicle (UUV) utilizing underwater robotic technology is an essential tool not only for harvesting ocean's natural resources but also for military applications, scientific explorations and even in search and rescue missions (Bleicher, 2010; Kinsey, Yoerger, Jakuba, Camilli, Fisher and German, 2011; Murphy, Dreger, Newsome, Rodocker, Steimle, Kimura, Makabe, Matsuno, Tadokoro and Kon, 2011; Søreide, 2011). Furthermore, ocean exploration involving manned underwater vehicle exposed the operator to extreme conditions which may be dangerous such as underwater pressure, visual visibility and oxygen supply problems. These operations are made possible without endangering human operators using the ability of underwater robots/vehicles to execute underwater intervention tasks.

In general, UUV can be classified into three types: remotely operated vehicles (ROVs), autonomous underwater vehicles (AUVs) and semi-autonomous underwater vehicles (semi-AUVs). ROVs are underwater vehicles that can be controlled by human operator from a remote position through master-slave system. Usually, a master controller is linked to the slave vehicle via tether. On the other hand, AUVs are non-tethered and autonomously controlled using pre-programmed control systems. While, semi-AUVs are vehicles that have both the ability

to be autonomously controlled or can be controlled via master-slave system. These three types of underwater vehicles are usually attached with underwater robotic manipulators for intervention tasks. This system is called underwater vehicle-manipulator system (UVMS).

One of the main issue in developing UVMSs is the control system. Unlike robots on land, underwater vehicles are not fixed on a physical location. The uncertain characteristics of hydrodynamic forces may affect the control performance of the vehicle especially the end-tips of the manipulators. Moreover, the needs of multiple robotic arms for efficient intervention operations made the design of the control system more complicated. Hydrodynamic reaction forces consisting of added mass and inertia produced from the motion of the manipulators may excite the motion of the vehicle, thus affecting the control precision of the manipulator's end-tips. Therefore, in order to produce a precise control of the end-tips, it is necessary to consider these problem in developing the control system of a UVMS (Fossen, 1995; Antonelli, 2003).

In the past three decades, a number of researchers have been focusing on the development of autonomous control system involving the coordinated motion control of UVMS (Maheshi, Yuh and Lakshmi, 1991; McLain, Rock and Lee, 1996; Antonelli, Caccavale, Chiaverini and Villani, 2000; Sarkar and Podder, 2001; Antonelli, 2003; Santhakumar and Jinwhan, 2012; Korkmaz, Ider and Ozgoren, 2013). However, there are only a few studies that have verified the effectiveness of their proposed methods through experiments. Furthermore, many of these control methods are based on computed torque control method. Using this method, the joints of the manipulator are controlled using the desired joint space signals that are transformed from the desired task space signals using only kinematic relation. However, the movement of the manipulator is affected by the motion of the body. Moreover, hydrodynamic forces due to added mass, added moment of inertia and drag will occur when a rigid body accelerates in underwater environment. Thus, the control performance will be highly affected by the performance of the vehicle. As a result, when the position error of the vehicle is large, inaccurate control of the end-tip will be obtained. Hence, it is extremely necessary to employ a control system that consider the coordinated motion of the vehicle and manipulators to improve the control of the end-tips. The authors have proposed digital Resolved Acceleration Control (RAC) method that can be utilized for 2-DOF planar single-arm and dual-arm UVMS (Sagara, Tamura, Yato and Shibuya, 2006; Bin Ambar, Sagara and Imai, 2014). In these works, the effectiveness of the proposed

method were demonstrated through numerical simulations and experimental results. Then, the proposed method was developed further for a 3-DOF 3-link dual-arm UVMS, and numerical simulations results showed good control performance (Sagara and Bin Ambar, 2014).

In this paper, the effectiveness of the proposed method is demonstrated through experimental results using a 3-link dual-arm UVMS in actual underwater environment. Using the proposed method, in spite of large position and attitude errors of the robot vehicle, good control performances of the arm's end-tips to follow a pre-planned trajectory can be achieved. The uniqueness of the proposed method is that the desired joint signals are obtained from kinematic and momentum equations utilizing feedback of task space signals consists of (a) the position and attitude of vehicle and end-tips, and also (b) linear and angular velocities of the vehicle and end-tips. Moreover, the method can reduce the influence of modeling errors of hydrodynamic forces using the position, attitude and velocity feedback of the UVMS.

MODELING OF UVMS

In this section, the mathematical model of a dual-arm UVMS including kinematics equation, momentum equation and equations of motion are described. The proposed RAC method is explained in the next section.

Fig. 1 shows the model of a dual-arm UVMS considered in this paper, consisting of the inertial coordinate frame Σ_I and vehicle coordinate frame Σ_0 . Here, Σ_I is introduced to describe the motion of the entire UVMS system. Symbols used in the model are defined as follows:

- n^* : number of joint of arm * (*=R: Right arm, *=L: Left arm)
- Σ_I : inertial coordinate frame
- Σ_0 : vehicle coordinate frame
- Σ_i^* : link i coordinate frame of arm * (*=R: Right arm, *=L: Left arm)
- ${}^iR_j^*$: coordinate transformation matrix from Σ_j^* to Σ_i^*
- p_e^* : position vector of manipulator end-tip with respect to Σ_I
- p_i^* : position vector of origin of Σ_i^* with respect to Σ_I
- r_0 : position vector of origin of Σ_0 with respect to Σ_I
- r_i^* : position vector of the center of mass for link i^* with respect to Σ_I
- ψ_0 : roll-pitch-yaw attitude vector of Σ_0 with respect to Σ_I
- ψ_e^* : roll-pitch-yaw attitude vector of end-tip of manipulator with respect to Σ_I
- ω_0 : angular velocity vector of origin of Σ_0 with respect to Σ_I
- ω_i^* : angular velocity vector of Σ_i^* with respect to Σ_I
- ω_e^* : angular velocity vector of manipulator end-tip with respect to Σ_I
- ϕ_i^* : relative angle of joint i^*
- ϕ : relative joint angle vector ($= [(\phi^R)^T, (\phi^L)^T]^T$), and $(\phi^* = [\phi_1^*, \phi_2^*, \dots, \phi_n^*]^T)$
- k_i^* : unit vector indicating a rotational axis of joint i^*
- m_0 : mass of vehicle (base)
- m_i^* : mass of link i^*
- $M_{a_i}^*$: added mass matrix of link i^* with respect to Σ_i^*
- I_i^* : inertia tensor of link i^* with respect to Σ_i^*
- $I_{a_i}^*$: added inertia tensor of link i^* with respect to Σ_i^*
- x_0 : position and attitude vector of Σ_0 with respect to Σ_I ($= [r_0^T, \psi_0^T]^T$)
- x_e^* : position and attitude vector of * manipulator end-tip with respect to Σ_I ($= [(p_e^*)^T, (\psi_e^*)^T]^T$)
- ν_0 : linear and angular vector of Σ_0 with respect to Σ_I ($= [\dot{r}_0^T, \dot{\omega}_0^T]^T$)
- ν_e^* : linear and angular vector of * manipulator end-tip with respect to Σ_I ($= [(p_e^*)^T, (\omega_e^*)^T]^T$)
- $a_{g_i}^*$: position vector from joint i^* to the center of mass for link i^* with respect to Σ_I
- $a_{b_i}^*$: position vector from joint i^* to buoyancy center of link i^* with

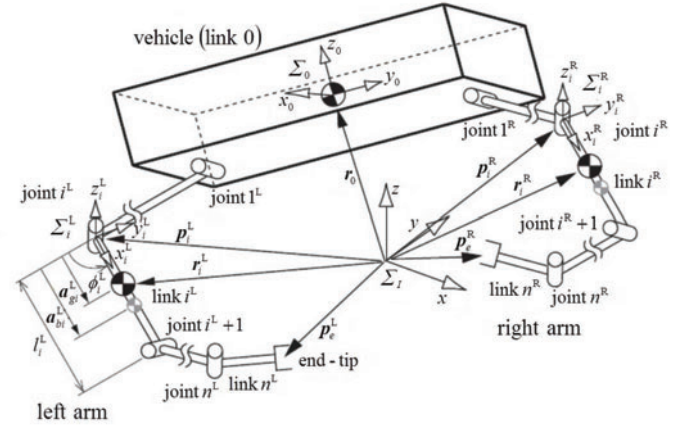


Fig. 1. Model of a dual-arm underwater robot

respect to Σ_I

l_i^* : length of link i^*

D_i^* : width of link i^*

V_i^* : volume of link i^*

ρ : fluid density

$C_{d_i}^*$: drag coefficient of link i^*

g : gravitational acceleration vector

E_j : $j \times j$ unit matrix

\tilde{r} : skew-symmetric matrix defined as

$$\tilde{r} = \begin{bmatrix} 0 & -z & y \\ z & 0 & -x \\ -y & x & 0 \end{bmatrix}, r = \begin{bmatrix} x \\ y \\ z \end{bmatrix}$$

Kinematics and Momentum Equations

The kinematics and momentum equations of the dual-arm UVMS are derived based on the work done in Sagara, Tamura, Yatoh and Shibuya (2006).

First, from Fig. 1, the end-tip velocity is derived based on the time derivative of the end-tip position vector p_e^* (* =R: Right arm, L: Left arm) as shown below:

$$\dot{p}_e^* = \dot{r}_0 + \tilde{\omega}_0(p_e^* - r_0) + \sum_{i=1}^n \{ \tilde{k}_i^*(p_e^* - p_i^*) \} \dot{\phi}_i^*. \quad (1)$$

Furthermore, the relationship between the end-tip angular velocity vector ω_e^* and joint velocities is expressed as

$$\omega_e^* = \omega_0 + \sum_{i=1}^n k_i^* \dot{\phi}_i^*. \quad (2)$$

From Eqs. (1) and (2) the following kinematics equation of the dual-arm UVMS is obtained:

$$\nu_e^* = A^* \nu_0 + B^* \dot{\phi}^* \quad (3)$$

where

$$A^* = \begin{bmatrix} E_3 & -(\tilde{p}_e^* - \tilde{r}_0) \\ 0 & E_3 \end{bmatrix}, \quad B^* = [b_1^* \quad b_2^* \quad \dots \quad b_n^*],$$

$$b_i^* = \begin{bmatrix} \tilde{k}_i^*(p_e^* - p_i^*) \\ k_i^* \end{bmatrix}.$$

Here, A and B are matrices consist of position and attitude of robot base and arm's joint angles, respectively.

Next, the momentum equation of the UVMS is consists of linear momentum of the UVMS (vehicle and manipulators) $\boldsymbol{\eta}$, and the angular momentum at the vehicle's center of mass $\boldsymbol{\mu}$. $\boldsymbol{\eta}$ and $\boldsymbol{\mu}$ are consist of hydrodynamic added mass tensor $\boldsymbol{M}_{a_i}^*$ and added inertia tensor $\boldsymbol{I}_{a_i}^*$ of link i^* , and are defined as follows

$$\boldsymbol{\eta} = \boldsymbol{M}_{T_0} \dot{\boldsymbol{r}}_0 + \boldsymbol{\eta}^R + \boldsymbol{\eta}^L, \quad (4)$$

$$\boldsymbol{\mu} = \boldsymbol{I}_{T_0} \boldsymbol{\omega}_0 + \tilde{\boldsymbol{r}}_0 \boldsymbol{M}_{T_0} \dot{\boldsymbol{r}}_0 + \boldsymbol{\mu}^R + \boldsymbol{\mu}^L \quad (5)$$

where

$$\boldsymbol{\eta}^* = \sum_{i=1}^{n^*} \boldsymbol{M}_{T_i}^* \dot{\boldsymbol{r}}_i^*, \quad \boldsymbol{\mu}^* = \sum_{i=1}^{n^*} \boldsymbol{I}_{T_i}^* \boldsymbol{\omega}_i^* + \tilde{\boldsymbol{r}}_i^* \boldsymbol{M}_{T_i}^* \dot{\boldsymbol{r}}_i^*,$$

$$\boldsymbol{M}_{T_0} = m_0 \boldsymbol{E}_3 + {}^I \boldsymbol{R}_0 \boldsymbol{M}_{a_0} {}^0 \boldsymbol{R}_I, \quad \boldsymbol{I}_{T_0} = {}^I \boldsymbol{R}_0 (\boldsymbol{I}_0 + \boldsymbol{I}_{a_0}) {}^0 \boldsymbol{R}_I,$$

$$\boldsymbol{M}_{T_i}^* = m_i^* \boldsymbol{E}_3 + {}^I \boldsymbol{R}_i^* \boldsymbol{M}_{a_i}^* {}^i \boldsymbol{R}_I^*, \quad \boldsymbol{I}_{T_i}^* = {}^I \boldsymbol{R}_i^* (\boldsymbol{I}_i^* + \boldsymbol{I}_{a_i}^*) {}^i \boldsymbol{R}_I^*$$

Here, linear and angular velocities at the center of mass for link i^* are described as

$$\dot{\boldsymbol{r}}_i^* = \dot{\boldsymbol{r}}_0 + \tilde{\boldsymbol{\omega}}_0 (\boldsymbol{r}_i^* - \boldsymbol{r}_0) + \boldsymbol{J}_{v_i}^* \dot{\boldsymbol{\phi}}^*, \quad (6)$$

$$\boldsymbol{\omega}_i^* = \boldsymbol{\omega}_0 + \boldsymbol{J}_{\omega_i}^* \dot{\boldsymbol{\phi}}^* \quad (7)$$

where

$$\boldsymbol{J}_{v_i}^* = \begin{bmatrix} \boldsymbol{j}_{i_1}^* & \boldsymbol{j}_{i_2}^* & \cdots & \boldsymbol{j}_{i_i}^* & \mathbf{0} & \cdots & \mathbf{0} \end{bmatrix},$$

$$\boldsymbol{J}_{\omega_i}^* = \begin{bmatrix} \boldsymbol{k}_1^* & \boldsymbol{k}_2^* & \cdots & \boldsymbol{k}_i^* & \mathbf{0} & \cdots & \mathbf{0} \end{bmatrix},$$

$$\boldsymbol{j}_{ij}^* = \boldsymbol{k}_j^* \times (\boldsymbol{r}_i^* - \boldsymbol{p}_j^*).$$

Therefore, from Eqs. (4)–(7), the following momentum equation for the UVMS is obtained:

$$\boldsymbol{s} = \begin{bmatrix} \boldsymbol{\eta} \\ \boldsymbol{\mu} \end{bmatrix} = \boldsymbol{C} \boldsymbol{\nu}_0 + \boldsymbol{D} \dot{\boldsymbol{\phi}} \quad (8)$$

where

$$\boldsymbol{C} = \begin{bmatrix} \boldsymbol{c}_{11} & \boldsymbol{c}_{12} \\ \boldsymbol{c}_{21} & \boldsymbol{c}_{22} \end{bmatrix},$$

$$\boldsymbol{D} = \begin{bmatrix} \boldsymbol{d}_{11}^R & \boldsymbol{d}_{12}^R & \cdots & \boldsymbol{d}_{1n^R}^R & \boldsymbol{d}_{11}^L & \boldsymbol{d}_{12}^L & \cdots & \boldsymbol{d}_{1n^L}^L \\ \boldsymbol{d}_{21}^R & \boldsymbol{d}_{22}^R & \cdots & \boldsymbol{d}_{2n^R}^R & \boldsymbol{d}_{21}^L & \boldsymbol{d}_{22}^L & \cdots & \boldsymbol{d}_{2n^L}^L \end{bmatrix},$$

$$\boldsymbol{c}_{11} = \boldsymbol{M}_{T_0} + \sum_{i=1}^{n^R} \boldsymbol{M}_{T_i}^R + \sum_{i=1}^{n^L} \boldsymbol{M}_{T_i}^L,$$

$$\boldsymbol{c}_{12} = -\sum_{i=1}^{n^R} \boldsymbol{M}_{T_i}^R (\tilde{\boldsymbol{r}}_i^R - \tilde{\boldsymbol{r}}_0) - \sum_{i=1}^{n^L} \boldsymbol{M}_{T_i}^L (\tilde{\boldsymbol{r}}_i^L - \tilde{\boldsymbol{r}}_0),$$

$$\boldsymbol{c}_{21} = -\tilde{\boldsymbol{r}}_0 \boldsymbol{M}_{T_0} + \sum_{i=1}^{n^R} \tilde{\boldsymbol{r}}_i^R \boldsymbol{M}_{T_i}^R + \sum_{i=1}^{n^L} \tilde{\boldsymbol{r}}_i^L \boldsymbol{M}_{T_i}^L,$$

$$\boldsymbol{c}_{22} = \boldsymbol{I}_{T_0} + \sum_{i=1}^{n^R} \boldsymbol{I}_{T_i}^R - \sum_{i=1}^{n^R} (\tilde{\boldsymbol{r}}_i^R - \tilde{\boldsymbol{r}}_0) \boldsymbol{M}_{T_i}^R (\tilde{\boldsymbol{r}}_i^R - \tilde{\boldsymbol{r}}_0)$$

$$+ \sum_{i=1}^{n^L} \boldsymbol{I}_{T_i}^L - \sum_{i=1}^{n^L} (\tilde{\boldsymbol{r}}_i^L - \tilde{\boldsymbol{r}}_0) \boldsymbol{M}_{T_i}^L (\tilde{\boldsymbol{r}}_i^L - \tilde{\boldsymbol{r}}_0),$$

$$\boldsymbol{d}_{1i}^* = \sum_{j=i}^{n^*} \boldsymbol{M}_{T_j}^* \tilde{\boldsymbol{k}}_i^* (\boldsymbol{r}_j^* - \boldsymbol{p}_i^*),$$

$$\boldsymbol{d}_{2i}^* = \sum_{j=i}^{n^*} \boldsymbol{I}_{T_j}^* \boldsymbol{k}_i^* + (\tilde{\boldsymbol{r}}_i^* - \tilde{\boldsymbol{r}}_0) \boldsymbol{M}_{T_j}^* \tilde{\boldsymbol{k}}_i^* (\boldsymbol{r}_j^* - \boldsymbol{p}_i^*).$$

Here, \boldsymbol{C} is matrix for mass and \boldsymbol{D} is matrix for inertia momentum. Both are included with hydrodynamic added mass and added inertia momentum which we assumed to be constant. In the real world, the added mass

and added inertia momentum are inconstant. However, this is compensated by using RAC method which will be introduced in the later section.

Equation of motion

First, the drag force and moment of joint i^* can be generally represented as follows (Levesque and Richard, 1994):

$$\boldsymbol{f}_{d_i}^* = \frac{\rho}{2} C_{D_i}^* D_i^* {}^I \boldsymbol{R}_i^* \int_0^{l_{i^*}} \|\boldsymbol{w}_i^*\| \boldsymbol{w}_i^* dx_i^*, \quad (9)$$

$$\boldsymbol{t}_{d_i}^* = \frac{\rho}{2} C_{D_i}^* D_i^* {}^I \boldsymbol{R}_i^* \int_0^{l_{i^*}} \hat{\boldsymbol{x}}_i^* \times \|\boldsymbol{w}_i^*\| \boldsymbol{w}_i^* dx_i^* \quad (10)$$

where

$$\boldsymbol{w}_i^* = \begin{bmatrix} 0 & \mathbf{0} \\ \mathbf{0} & \boldsymbol{E}_2 \end{bmatrix} {}^i \boldsymbol{R}_I^* (\dot{\boldsymbol{r}}_i^* + \tilde{\boldsymbol{\omega}}_i^* \hat{\boldsymbol{x}}_i^*), \quad \hat{\boldsymbol{x}}_i^* = \begin{bmatrix} x_i^* \\ 0 \\ 0 \end{bmatrix}.$$

Next, the gravitational and buoyant forces acting link i^* are described as follows:

$$\boldsymbol{f}_{g_i}^* = (\rho V_i^* - m_i^*) \boldsymbol{g}, \quad (11)$$

$$\boldsymbol{t}_{g_i}^* = (\rho V_i^* \tilde{\boldsymbol{a}}_{b_i} - m_i^* \tilde{\boldsymbol{a}}_{g_i}) \boldsymbol{g}. \quad (12)$$

Taking into account the effect of the hydrodynamic forces described above and using recursive Newton-Euler formulation described by Antonelli (2003), the following equations of motion can be obtained:

$$\boldsymbol{M}(\boldsymbol{q}) \dot{\boldsymbol{\zeta}} + \boldsymbol{N}(\boldsymbol{q}, \boldsymbol{\zeta}) \boldsymbol{\zeta} + \boldsymbol{f}_D = \boldsymbol{u} \quad (13)$$

where $\boldsymbol{q}^T = [\boldsymbol{r}_0^T, \boldsymbol{\psi}_0^T, \boldsymbol{\phi}^T]$ and $\boldsymbol{\zeta}^T = [\boldsymbol{\nu}_0^T, \dot{\boldsymbol{\phi}}^T]$, $\boldsymbol{M}(\boldsymbol{q})$ is the inertia matrix consists of added mass $\boldsymbol{M}_{a_i}^*$ and inertia $\boldsymbol{I}_{a_i}^*$, $\boldsymbol{N}(\boldsymbol{q}, \boldsymbol{\zeta})$ is the vector of Coriolis and centrifugal forces, and \boldsymbol{f}_D is the vector consists of drag, gravitational and buoyant forces and moments. \boldsymbol{u} is the input vector consisting of force and torque vectors provided by thrusters and joint torques, where $\boldsymbol{u} = [\boldsymbol{f}_0^T, \boldsymbol{\tau}_0^T, \boldsymbol{\tau}_m^T]^T$. \boldsymbol{f}_0^T and $\boldsymbol{\tau}_0^T$ are the force and torque vectors of the robot, $\boldsymbol{\tau}_m^T$ is the torque vector for arm joints. Furthermore, the relationship between $\boldsymbol{\omega}_{\dagger}$ and $\dot{\boldsymbol{\psi}}_{\dagger} = [\dot{\psi}_{r_{\dagger}}, \dot{\psi}_{p_{\dagger}}, \dot{\psi}_{y_{\dagger}}]^T$ ($\dagger = 0, e_R, e_L$) is described as

$$\boldsymbol{\omega}_{\dagger} = \boldsymbol{S}_{\psi_{\dagger}} \dot{\boldsymbol{\psi}}_{\dagger} \quad (14)$$

where

$$\boldsymbol{S}_{\psi_{\dagger}} = \begin{bmatrix} \cos \psi_{p_{\dagger}} \cos \psi_{p_{\dagger}} & -\sin \psi_{y_{\dagger}} & 0 \\ \cos \psi_{p_{\dagger}} \sin \psi_{p_{\dagger}} & \cos \psi_{y_{\dagger}} & 0 \\ \sin \psi_{p_{\dagger}} & 0 & 1 \end{bmatrix}.$$

Thus the relationship between $\dot{\boldsymbol{q}}$ and $\boldsymbol{\zeta}$ is described as

$$\boldsymbol{\zeta} = \boldsymbol{S} \dot{\boldsymbol{q}} \quad (15)$$

where $\boldsymbol{S} = \text{blockdiag} \{ \boldsymbol{E}_3, \boldsymbol{S}_{\psi_0}, \boldsymbol{E}_{(n^R+n^L)} \}$.

RESOLVED ACCELERATION CONTROL (RAC)

As mentioned in previous section, the RAC is a control method that determine the control input which consists of force and torque of vehicle and arm's joint torque based on the desired acceleration, velocity and position of the UVMS. The method utilizes the kinematic and momentum equations using feedback of task space signals consisting of (a) the position and attitude of vehicle and end-tips, and also (b) linear and angular velocities of the vehicle and end-tips.

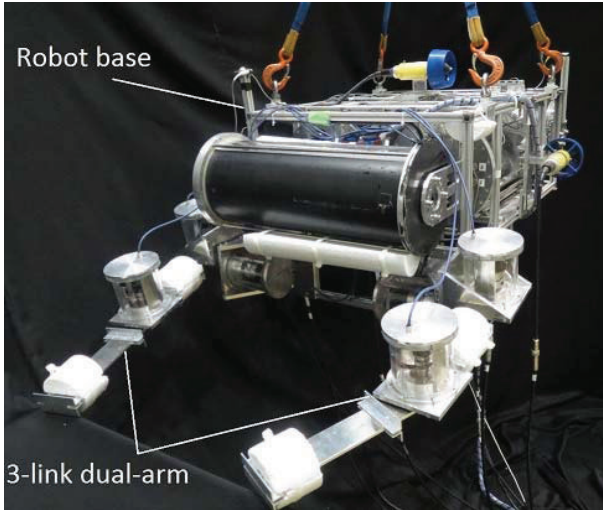


Fig. 2. 3-link dual-arm UVMS

The relationship between the desired velocities of vehicle and arm's end-tips β and the required vehicle acceleration and arm joints angular acceleration α can be expressed by differentiating Eqs. (3) and (8) with respect to time. As a result, the following equation can be obtained:

$$\mathbf{W}(t)\alpha(t) = \beta(t) + \mathbf{f}(t) - \dot{\mathbf{W}}(t)\mathbf{v}(t) \quad (16)$$

where

$$\mathbf{W} = \begin{bmatrix} \mathbf{C} + \mathbf{E}_6 & \mathbf{D} \\ \mathbf{A} & \mathbf{B} \end{bmatrix}, \quad \alpha = \begin{bmatrix} \dot{\nu}_0 \\ \dot{\phi} \end{bmatrix}, \quad \beta = \begin{bmatrix} \dot{\nu}_0 \\ \dot{\nu}_e \end{bmatrix},$$

$$\mathbf{f} = \begin{bmatrix} \dot{\mathbf{s}} \\ \mathbf{0} \end{bmatrix}, \quad \mathbf{v} = \begin{bmatrix} \nu_0 \\ \dot{\phi} \end{bmatrix}, \quad \dot{\phi} = \begin{bmatrix} \dot{\phi}^R \\ \dot{\phi}^L \end{bmatrix}, \quad \dot{\nu}_e = \begin{bmatrix} \dot{\nu}_e^R \\ \dot{\nu}_e^L \end{bmatrix},$$

$$\mathbf{A} = \begin{bmatrix} \mathbf{A}^R \\ \mathbf{A}^L \end{bmatrix}, \quad \mathbf{B} = \begin{bmatrix} \mathbf{B}^R & \mathbf{0} \\ \mathbf{0} & \mathbf{B}^L \end{bmatrix}$$

and \mathbf{s} is the external force including hydrodynamic force and thrust of the thruster which act on the base.

Then, Eq. (16) is discretized with sampling period T , and by applying $\beta(t)$ and $\dot{\mathbf{W}}(t)$ to the backward Euler approximation, the following equation can be obtained:

$$T\mathbf{W}(k)\alpha(k-1) = \nu(k) - \nu(k-1) + T\mathbf{f}(k) - \{\mathbf{W}(k) - \mathbf{W}(k-1)\}\mathbf{v}(k) \quad (17)$$

where $\nu = [\nu_0^T, \nu_e^T]^T$. Note that computational time delay is introduced to Eq. (17), and the discrete time kT is abbreviated to k .

Table 1. Physical parameters of underwater robot

	Base	Link 1	Link 2	Link 3
Mass [kg]	104.52	5.90	2.86	1.40
Moment of inertia (x axis) [kgm ²]	2.4	7.933 × 10 ⁻³	3.575 × 10 ⁻³	1.75 × 10 ⁻³
Moment of inertia (y axis) [kgm ²]	2.4	7.933 × 10 ⁻³	23.24 × 10 ⁻³	13.97 × 10 ⁻³
Moment of inertia (z axis) [kgm ²]	2.4	7.368 × 10 ⁻³	23.24 × 10 ⁻³	13.97 × 10 ⁻³
Link length (x axis) [m]	0.870	0.093	0.305	0.335
Link length (y axis) [m]	0.640	-	-	-
Link length (z axis) [m]	0.335	-	-	-
Link diameter[m]	-	0.10	0.10	0.10
Added mass(x) [kg]	73.19	0.730	0.333	0.333
Added mass(y) [kg]	30.57	0.730	2.356	2.631
Added mass(z) [kg]	99.54	0.333	2.356	2.631
Added moment of inertia (x) [kgm ²]	0.64	0.077 × 10 ⁻³	2.454 × 10 ⁻³	2.454 × 10 ⁻³
Added moment of inertia (y) [kgm ²]	1.28	0.077 × 10 ⁻³	27 × 10 ⁻³	46.88 × 10 ⁻³
Added moment of inertia (z) [kgm ²]	0.64	2.4 × 10 ⁻³	27 × 10 ⁻³	46.88 × 10 ⁻³
Drag coefficient(x)	1.2	1.0	1.0	1.0
Drag coefficient(y)	1.2	1.0	1.0	1.0
Drag coefficient(z)	1.2	1.0	1.0	1.0

From Eq. (17) the desired acceleration (resolved acceleration) for the robot base and desired angular of both arm's joints $\alpha_d(k)$ is defined as follows:

$$\alpha_d(k) = \frac{1}{T}\mathbf{W}(k)^+ \{\nu_d(k+1) - \nu_d(k) + \mathbf{A}e_\nu(k) + T\mathbf{f}(k)\}. \quad (18)$$

Moreover, the desired velocity for the robot base and both arm's end-tips $\nu_d(k)$ is defined as follows:

$$\nu_d(k) = \frac{\mathbf{S}_{0e}}{T} \{\mathbf{x}_d(k) - \mathbf{x}_d(k-1) + \mathbf{\Gamma}e_x(k-1)\} \quad (19)$$

where $e_\nu(k) = \nu_d(k) - \nu(k)$, $e_x(k) = \mathbf{x}_d(k) - \mathbf{x}(k)$ and $\mathbf{S}_{0e} = \text{blockdiag}\{\mathbf{E}_3, \mathbf{S}_{\psi 0}, \mathbf{E}_3, \mathbf{S}_{\psi e_R}, \mathbf{E}_3, \mathbf{S}_{\psi e_L}\}$. $\mathbf{W}(k)^+$ is the pseudoinverse of \mathbf{W} , \mathbf{x}_d is the desired value of $\mathbf{x} = [\mathbf{x}_0^T, (\mathbf{x}_0^R)^T, (\mathbf{x}_0^L)^T]^T$. $\mathbf{A} = \text{diag}\{\lambda_i\}$ is the position error and attitude error feedback gain matrices. $\mathbf{\Gamma} = \text{diag}\{\gamma_i\}$ is the linear and angular velocity error feedback gain matrices. Here, $i=1, \dots, 18$ (robot base DOF + joints DOF).

From Eqs. (17), (18) and (19), if λ_i and γ_i are selected to satisfy $0 < \lambda_i < 1$ and $0 < \gamma_i < 1$, respectively, and the convergence of the acceleration error, $e_\alpha(k) = \alpha_d(k) - \alpha(k)$, tends to zero as k tends to infinity, then the convergence of $e_\nu(k)$ and $e_x(k)$ to zero as k tends to infinity can be ensured.

EXPERIMENTS AND RESULTS

This section describes the experiments to verify the effectiveness of the proposed control system using an actual 3-link dual-arm UVMS shown in Fig. 2. Table 1 shows the physical parameters of the UVMS.

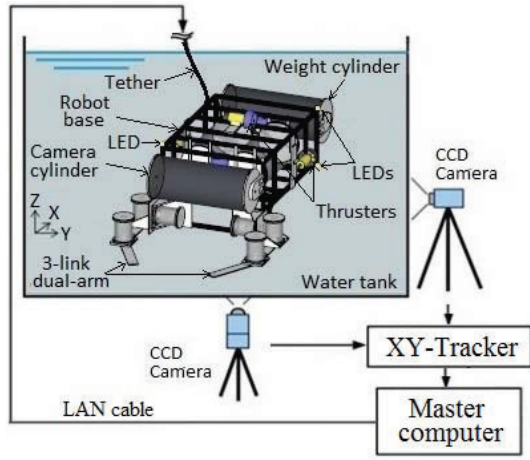


Fig. 3. Experimental setup

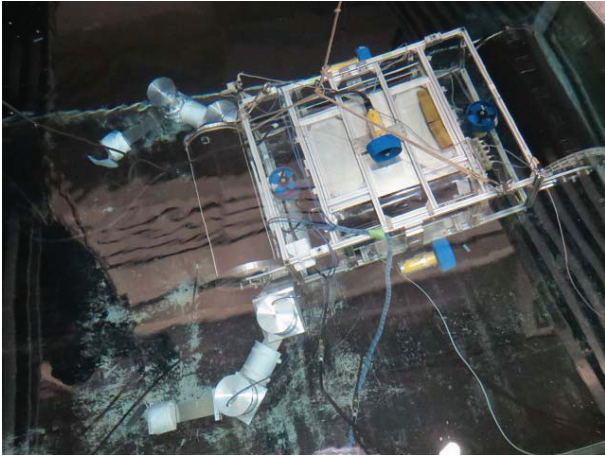


Fig. 4. UVMS floating inside a water tank

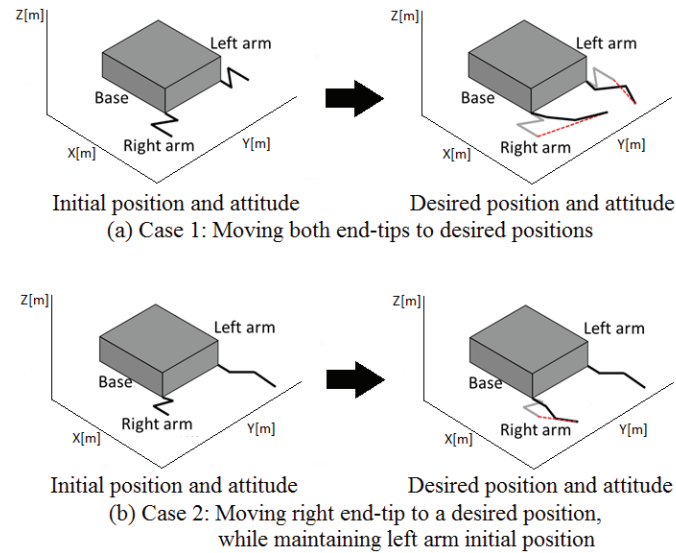


Fig. 5: Animation representation of two cases for experimenting the effectiveness of the proposed RAC method. Red dashed lines on the right animation of both cases show the desired path of the end-tips.

Experimental System

Fig. 3 shows the experimental setup in this work. The experiments were carried out in a water tank with a length of 2[m], width of 3[m] and depth of 2[m]. The water tank has glass windows on the front and side that enables researchers to view the condition of the UVMS during experiments. Fig. 4 shows an image of the actual UVMS floating inside the water tank. The position, attitude and velocity of the robot can be calculated by monitoring the movement of three LEDs light sources via CCD cameras as shown in Fig. 3. First, the data from CCD cameras were converted to position data using an X-Y video tracker (with a processing speed of 1/60[s]). Then, these information are sent to a master computer via a GPIB communication line. Based on the position data and rotational angle of each joint measured by the encoder inside the servo motors, the positions and attitude angles of the robot base and dual-arms are computed in the master computer, and also used in the proposed RAC method. Finally, the master computer sent the desired informations to a robot computer installed inside the robot base via LAN cable.

The main structure of the robot base are made from Bosch aluminum frames. The robot base is capable to move in 3-dimensional space using six units of DC motor driven single-propeller thrusters from Mitsui Engineering and Shipbuilding. The 40[W] thrusters are installed in the vertical, horizontal and lateral directions on the robot base in pairs, to provide propulsion for controlling the position and attitude angle of the robot base. This configuration of thrusters enables tasks in confined areas such as the water tank in this work. Each thrusters is capable to produce a maximum of about 16[N] of thrust force. In order to control the rotational speed of these thrusters, voltage signal inputs from the master computer were initially sent to two units of dsPIC30F3011 microcontrollers from Microchip Technology. These microcontrollers process the voltage signals into pulse-width-modulation (PWM) control single input to be sent to each thrusters drivers that controls the rotational speed of the thrusters.

In order to control the joints motion of the dual-arm, the servo motors inside the joints are connected to the robot computer via an FPGA. The servo motors are connected to the FPGA via RS-485 communication line. Then, the FPGA is connected to the master computer via RS-232C communication line. Each joint of the dual-arm utilized a B3M series command-type servo motor from Kondo Kagaku Company Limited. The current angles and angular velocities of the joints are derived using the output values from the encoder located inside the servo motors. These output values are sent to the master computer that calculates these information into control inputs for the robot, and also provided the command input to drive each servo motor.

Experimental Condition and Methods

The experiments were carried out under the following conditions. The position error feedback gains \mathbf{I} and velocity error feedback gains \mathbf{A} for the robot base and manipulators were $\mathbf{I} = \text{diag}\{0.025 \ 0.03 \ 0.025 \ 0.06 \ 0.055 \ 0.05 \ 0.06 \ 0.06 \ 0.06 \ 0 \ 0 \ 0 \ 0.06 \ 0.06 \ 0.06 \ 0 \ 0 \ 0\}$ and $\mathbf{A} = \text{diag}\{0.001 \ 0.005 \ 0.004 \ 0.002 \ 0.004 \ 0.005 \ 0.1 \ 0.1 \ 0 \ 0 \ 0 \ 0.1 \ 0.1 \ 0 \ 0 \ 0\}$. The data sampling period was $T = 1/20[\text{s}]$. As the robot base needed to be in station keeping condition during the experiments, the initial position and attitude of the robot base was $[0, 0, 0][\text{m}]$ and $[0, 0, 0][\text{rad}]$. The robot base has a maximum translational speed of 0.05[m/s], maximum rotational speed of $\pi/18[\text{rad/s}]$, translational acceleration of 0.0083[m/s²] and rotational acceleration of $\pi/72[\text{rad/s}^2]$. The RAC method is estimated to enable the control of end-tips of both manipulators robot base by considering the external forces. Thus, we assumed that the RAC method may reduce the errors between the actual and desired positions and attitude of the end-tips. There are two cases of experiments that were carried out in this work, as shown in Fig. 5.

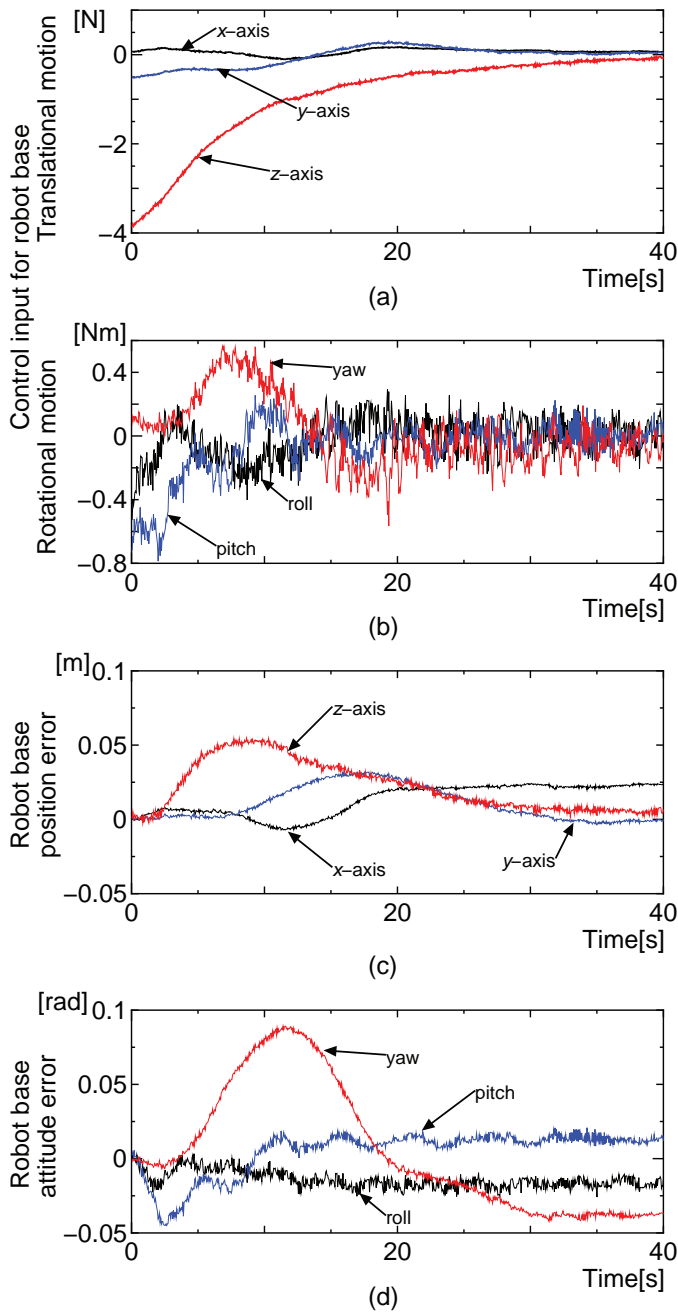


Fig. 6. Experimental results for case 1: robot base position and attitude

First, in case 1 shown in Fig. 5(a), both arms were moved to desired positions, as if it was reaching a target object in front of the robot. The initial angle for the first, second and third joints of the right manipulator were $0[\text{deg}]$, $-100[\text{deg}]$ and $100[\text{deg}]$. While, the initial angle for the first, second and third joints of the left manipulator were $0[\text{deg}]$, $100[\text{deg}]$ and $-100[\text{deg}]$. In this experiment, the desired end-tip positions were set up along a straight path from the initial positions to the desired positions. At the same time, the robot base was in station-keeping condition. The desired end-tip positions of both right and left manipulators were $[-0.2, -0.5, -0.3][\text{m}]$ and $[-0.2, 0.1, -0.2][\text{m}]$. The desired position and attitude of the robot base were the same as the initial position and attitude.

Next, in case 2 shown in Fig. 5(b), while the left arm was holding its initial position, the right arm was moved to a desired position, as if it was

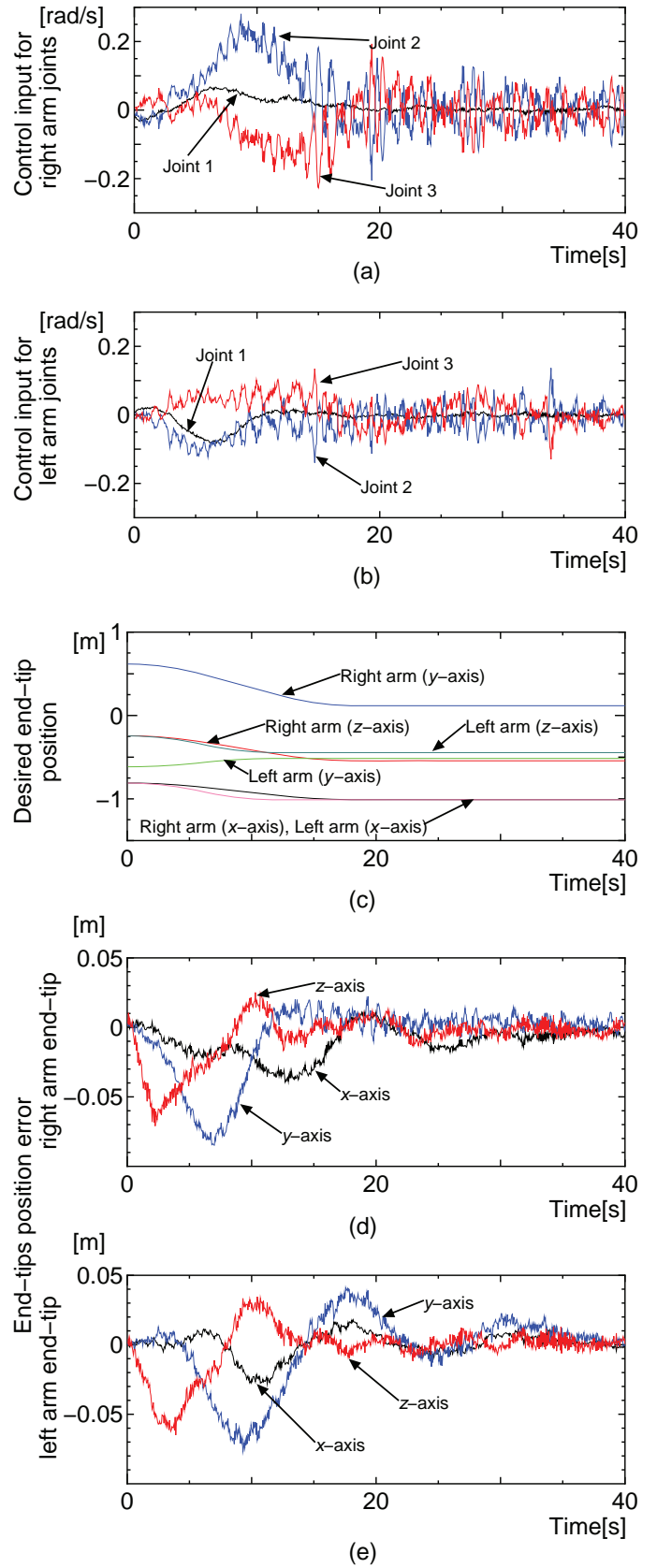


Fig. 7. Experimental results for case 1: end-tip positions

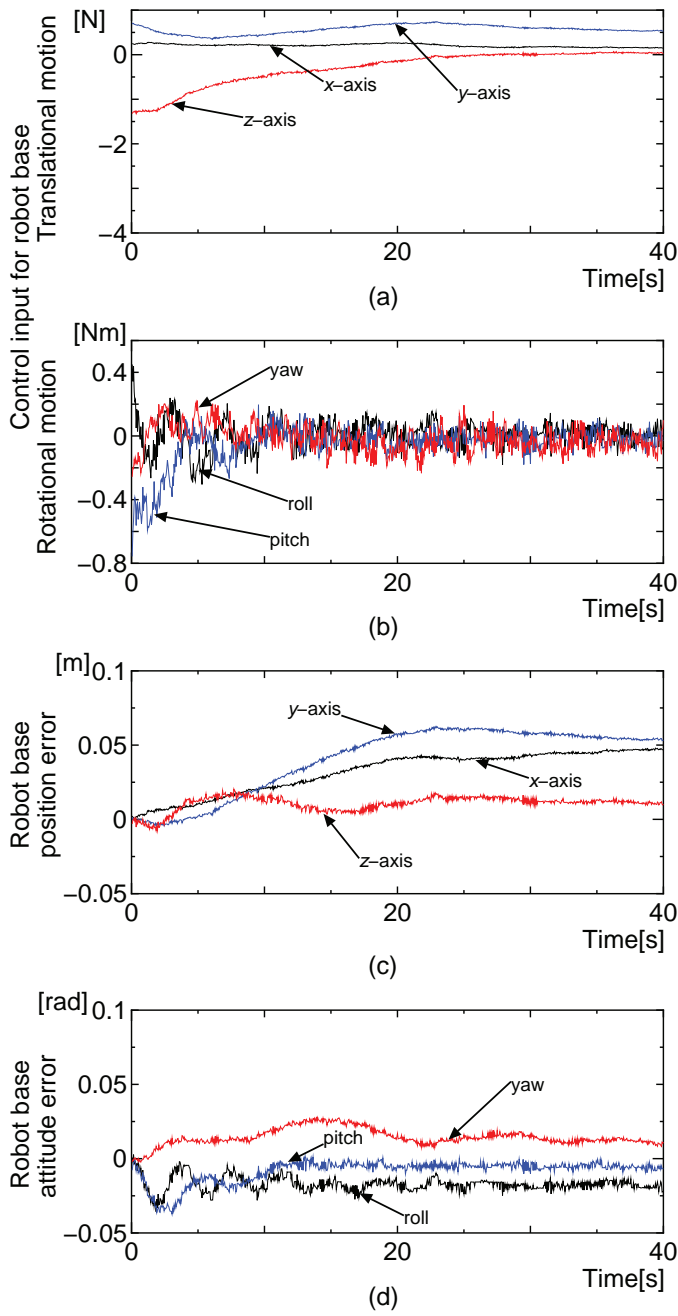


Fig. 8. Experimental results for case 2: robot base position and attitude

reaching a target object. The initial angle for the first, second and third joints of the right manipulator were $-30[\text{deg}]$, $-100[\text{deg}]$ and $100[\text{deg}]$. While, the initial angle for the first, second and third joints of the left manipulator were $0[\text{deg}]$, $45[\text{deg}]$ and $-60[\text{deg}]$. The desired end-tip position of the right arm was set up along a straight path from the initial position to the desired positions. At the same time, the desired end-tip position of the left arm was kept the same as the initial position, and the robot base was in station-keeping condition. The desired end-tip positions of both right and left arm's end-tips were at $[-0.3, -0.3, -0.3][\text{m}]$ and $[0, 0, 0][\text{m}]$. The desired position and attitude of the robot base were the same as the initial position and attitude.

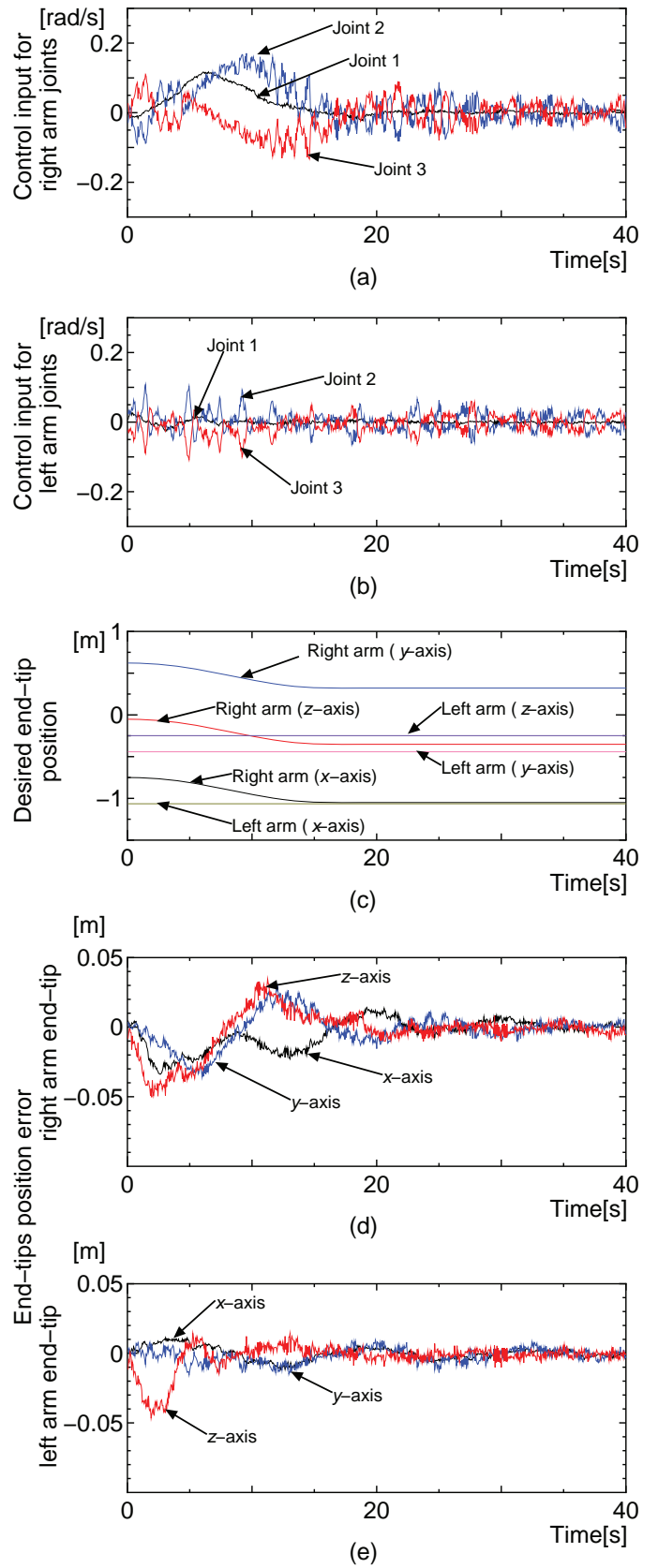


Fig. 9. Experimental results for case 2: end-tip positions

Experimental Results

In Fig. 6, data for robot base position and attitude error from experiment for case 1 are shown. Fig. 7 shows data related to both arm end-tips performances from experiment for case 1. Firstly, Fig. 6(a) and (b) show the thrusters control inputs for the robot base translational and rotational motions. Both of these figures show the thrust forces that were required to counteract the forces generated from both arm movements. Fig. 6(c) shows the robot base position errors on x , y and z axes during the movement of the arms. The figure shows that the robot base was able to maintain position errors within ± 0.05 [m]. Fig. 6(d) shows the robot base attitude errors during the movement of the arms. The figure also shows that the attitude errors was within ± 0.1 [rad] which is quite large due to the motion of both arm that was moving simultaneously to the desired end-tip positions. Fig. 7(a) and (b) show the control input for the right arm and left arm joints. In this work, the arm joints required velocity input rather than position input in order to move the actuators. By using velocity input, the errors while calculating the desired acceleration can be reduced. Fig. 7(c) shows a time history of the positions of the end-tips of both left and right manipulators moving from the initial positions to the desired positions. Fig. 7(d) and (e) show the end-tips position errors for both right and left arm. The figures show that even though the UVMS motion was under the influence of hydrodynamic forces due to the coupled effects of robot base and dual-arm, both end-tips were able to follow the desired trajectories to reach the desired positions with the maximum position error of about ± 0.03 [m]. Moreover, although the robot base position and attitude error were large as shown in Fig. 6(c) and (d), after 20[s], the position error of the end-tips were successfully reduced to within ± 0.01 [m].

Fig. 8(a) to (i) show the results for robot base position and attitude error from experiment for case 2. Fig. 8(a) and (b) show the thrusters control inputs for the robot base translational and rotational motions. Fig. 8(c) shows the robot base position errors on x , y and z axes during the movement of the arms for case 2. The figure shows that the robot base was moving significantly on x and y axes due to the influence of the arms motion towards the desired end-tip position. Fig. 8(d) shows the robot base attitude errors during the movement of the right arm. The figure also shows that the attitude errors was within ± 0.04 [rad] which is quite small despite the right arm motion. Fig. 9(a) and (b) show the control input for the right arm and left arm joints. Fig. 9(c) shows a time history of the positions of the end-tip of the right arm moving from the initial positions to the desired positions, at the same time the left arm kept the initial position. Fig. 9(d) and (e) show the end-tips position errors for both right and left arm. Similar to the results acquired from experiment for case 1, even though the UVMS motion was under the influence of hydrodynamic forces due to the coupled effects of robot base and dual-arm, both end-tips were able to follow the desired trajectories to reach the desired positions with the maximum position error of about ± 0.03 [m]. After 20[s], the position error of the end-tips were further reduced to within ± 0.01 [m], in spite of the considerable deviations in the robot base's position and attitude as shown in Fig. 8(c) and (d).

CONCLUSIONS

In this paper, a resolved acceleration control method has been developed for coordinated motion control of an underwater vehicle equipped with manipulators. Based on two cases of experiment results described in this paper, the proposed method was able to provide good control performances of the arm's end-tips to follow the pre-planned trajectories, in spite of hydrodynamic forces due to the coupled effects of robot base and dual-arm, and large position and attitude errors of the underwater vehicle.

There are several exciting future studies that can be carried out follow-

ing the positive results achieved in this work. Currently, the position and attitude of the robot are depended on X-Y video tracker. Thus, upgrading it to commercial off-the-shelf inertial measurement unit (IMU) can provide a more precise control of the robot and simplify the experimental setup. Moreover, the developed underwater vehicle is a type of semi-autonomous underwater vehicle (semi-AUV) that is suitable for underwater intervention tasks. Therefore, a master-slave system can be developed for the semi-AUV, utilizing human-robot interface to an autonomous underwater vehicle system. As a result, the performance of the underwater vehicle can be improved by maintaining the ability of direct human intervention in an autonomous robotic system. Furthermore, the development of hand grippers for the dual-arm are necessary for future underwater intervention tasks.

REFERENCES

- Antonelli, G, Caccavale, F, Chiaverini, S, and Villani, L (2000). "Tracking Control for Underwater Vehicle-Manipulator Systems with Velocity Estimation," *IEEE J Oceanic Eng*, 25(3), 399 – 413.
- Antonelli, G (2003). *Underwater Robots*, Springer, 1194 – 1206.
- Bin Ambar, R, Sagara, S, and Imai, K (2014) "Experiment on a dual-arm underwater robot using resolved acceleration control method," *J. Artificial Life and Robotics*, Springer, DOI:10.1007/s10015-014-0192-7.
- Bleicher, A (2010). "The Gulf spill's lessons for robotics," *IEEE Spectrum*, Vol. 47, No. 3, 9 – 11.
- Fossen, TI (1995). "Guidance and Control of Ocean Vehicles," *John Wiley & Sons*, 431–452.
- Kinsey, JC, Yoerger, DR, Jakuba, MV, Camilli, R, Fisher, CR, German, CR (2011). "Assessing the Deepwater Horizon oil spill with the sentry autonomous underwater vehicle," *Proc 2011 IEEE/RSJ Int Conf on Intelligent Robots and Systems*, 261 – 267.
- Korkmaz, O, Ider, SK, Ozgoren, MK (2013). "Control of an underactuated underwater vehicle manipulator system in the presence of parametric uncertainty and disturbance," *Proc. of American Control Conference (ACC)*, 578 – 584.
- Levesque, B, and Richard, MJ (1994). "Dynamic Analysis of a Manipulator in a Fluid Environment," *Int J Robotics Research*, 13(3), 221–231.
- Maheshi, H, Yuh, J, and Lakshmi, R (1991). "A Coordinated Control of an Underwater Vehicle and Robotic Manipulator," *J Robotic Systems*, 8(3), 339 – 370.
- McLain, TW, Rock, SM, and Lee MJ (1996) "Experiments in the Coordinated Control of an Underwater Arm/Vehicle System," *Autonomous Robots*, 3, Kluwer Academic Publishers, 213 – 232.
- Murphy, RR, Dreger, KL., Newsome, S, Rodocker, J, Steimle, E, Kimura, T, Makabe, K, Matsuno, F, Tadokoro, and S, Kon, K (2011). "Use of remotely operated marine vehicles at Minamisanriku and Rikuzentakata Japan for disaster recovery," *Proc 2011 IEEE Int Symp on Safety, Security, and Rescue Robotics*, 19 – 25.
- Sagara, S, Tamura, M, Yatoh, T, and Shibuya, K (2006). "Digital RAC for Underwater Vehicle-Manipulator Systems Considering Singular Configuration," *Artificial Life and Robotics*, Springer, 10(2), 106 – 111.
- Sagara, S, and Bin Ambar, R (2014) "Digital Resolved Acceleration Control of Underwater Robot with multiple manipulators," *Proc 2014 Int Conf on Advanced Mechatronic Systems*, Kumamoto, 232 – 237.
- Sarkar, N, and Podder, TK (2001). "Coordinated Motion Planning and Control of Autonomous Underwater Vehicle-Manipulator Systems Subject to Drag Optimization," *IEEE J Oceanic Eng*, 26(2), 228 – 239.
- Santhakumar, M, and Jinwhan, K (2012). "Indirect adaptive control of an autonomous underwater vehicle-manipulator system for underwater manipulation tasks," *Ocean Engineering*, 54, 233 – 243.
- Sørdeide, F (2011). "Ships from the Depths: Deepwater Archaeology," *Texas A & M University Press*, 29 – 40.